Journal of Materials Chemistry A

Materials for energy and sustainability

Accepted Manuscript

Journal of
Materials Chemistry A

Materials for energy and sustainability

rsc.li/materials-a

Volume 6
Number 12
28 March 2018
Pages 4883-5230

ISSN 2050-7488

ROYAL SOCIETY OF CHEMISTRY

COMMUNICATION
Zhemai Wen *et al.*
An electrochemically neutralized energy-assisted low-cost acid-alkaline electrolyzer for energy-saving electrolysis hydrogen generation

This is an Accepted Manuscript, which has been through the Royal Society of Chemistry peer review process and has been accepted for publication.

Accepted Manuscripts are published online shortly after acceptance, before technical editing, formatting and proof reading. Using this free service, authors can make their results available to the community, in citable form, before we publish the edited article. We will replace this Accepted Manuscript with the edited and formatted Advance Article as soon as it is available.

You can find more information about Accepted Manuscripts in the Information for Authors.

Please note that technical editing may introduce minor changes to the text and/or graphics, which may alter content. The journal's standard Terms & Conditions and the Ethical guidelines still apply. In no event shall the Royal Society of Chemistry be held responsible for any errors or omissions in this Accepted Manuscript or any consequences arising from the use of any information it contains.

ROYAL SOCIETY OF CHEMISTRY

rsc.li/materials-a

Penta-OsP₂ and Penta-RhS₂ Sheets Derived from Marcasite and Pyrite with Low Lattice Thermal Conductivity†

Yiheng Shen,[a] Jie Sun,[a] Yanyan Chen,[a] Dongyuan Ni,[a] Tingwei Li,[a] Akira Yoshikawa,[b]   Yoshiyuki Kawazoe,[c] and Qian Wang*[a]

[a] CAPT, School of Materials Science and Engineering, BKL-MEMD, Peking University, Beijing 100871, China.

[b] Institute for Materials Research, Tohoku University, Sendai, 980-8577, Japan;

[c] New Industry Creation Hatchery Center, Tohoku University, Sendai, 980-8577, Japan; Department of Physics, Suranaree University of Technology, 30000 Nakhon Ratchasima, Thailand; Department of Physics and Nanotechnology, SRM Institute of Science and Technology, Kattankulathur, Tamil Nadu 603203, India.

* Author to whom any correspondence should be addressed: qianwang2@pku.edu.cn

† Electronic supplementary information (ESI) available.

Abstract

Inspired by the experimental synthesis of penta-FeS₂ sheet from chemically cleaving bulk iron pyrite via liquid-phase exfoliation, going beyond the reported mechanical exfoliation, chemical vapor deposition, molecular beam epitaxy and high-pressure method, in this work, we theoretically demonstrate that stable penta-OsP₂ and penta-RhS₂ sheets can also be chemically exfoliated from the existing bulk marcasite and pyrite materials. We show that the resulting penta-sheets have monoclinic symmetry, which has not been seen in any binary penta-sheets reported so far. Penta-OsP₂ and penta-RhS₂ possess weak harmonicity and strong anharmonicity because of the low symmetry of their geometric configurations and the heavy transition elements in their compositions, as revealed by a detailed analysis of their phonon group velocities, three-phonon phase spaces, Grüneisen parameters and three-phonon scattering rates based on density functional theory and phonon Boltzmann transport theory. The strong phonon scattering in the penta-OsP₂ and penta-RhS₂ sheets leads to low lattice thermal conductivities of 3.19 and 2.90 W·m⁻¹·K⁻¹ at 300 K, and the optimized *ZT* values of 1.21 and 1.33, respectively. The lattice thermal conductivities and the optimized *ZT* values are an order of magnitude lower and higher than those of penta-PdS₂, respectively. These findings expand the family of pentagon-based sheets in geometry, chemical composition, and functionality.

1. Introduction

Since the proposal of penta-graphene,[1] a pentagon-based two-dimensional (2D) carbon allotrope, a family of over 100 pentagon-based 2D materials has been reported with novel physical properties and vast potential applications.[2,3] For instance, negative Poisson's ratio (NPR) has been found in penta-BN_2,[4,5] penta-ZnO_2,[6] and penta-$PdSe_2$,[7,8] topological electronic states have been reported in penta-RuS_4,[9] MoS_2,[10] and p-PbS_2,[11] ferromagnetism and antiferromagnetism have been found in penta-MnN_2,[12] and CoS_2,[13] ferroelasticity was reported in penta-PdS_2,[14] piezoelectric responses have been found in penta-BCN,[15,16] penta-CNP[17] and some transition metal-based ternary pentagonal sheets,[18] and second harmonic generation was predicted in penta-ZnS_2.[19] Meanwhile, considerable effort has been made to synthesize such pentagon-based materials. As a result, penta-silicene nanoribbon was synthesized via physical vapor deposition.[20] Penta-$PdSe_2$ has been prepared by using different techniques, including mechanical exfoliation,[21,22] chemical vapor deposition[23] and molecular beam epitaxy.[24] Penta-PdS_2 was fabricated by sulfurization of Pd film.[25] Penta-NiN_2 was synthesized at high pressure.[26] Recently, the theoretically predicted penta-FeS_2[27] was synthesized via liquid-phase exfoliation of iron pyrite,[28] which not only provides a new route to synthesize pentagon-based sheets, but also shows that the liquid-phase exfoliation is powerful enough to break the chemical bonds between transition metal and p-block atoms, so that the non-layered compounds can be exfoliated into thin layers with pentagonal configurations. Motivated by these advances, we explore the possibility of designing new pentagon-based 2D sheets from the top-down approach by chemical

cleaving bulk materials with internal pentagonal configurations, including marcasite and pyrite materials, which are both recognized as bulk precursors of binary pentagon-based 2D materials in precious reports.[27,29-31]

On the other hand, 2D pentagonal materials usually possess low lattice thermal conductivities due to their complex geometric structures as compared to their hexagonal counterparts, especially for the penta-sheets containing heavy atoms. For instance, it was found that penta-Sb_2C possesses an ultralow lattice thermal conductivity of 0.72 $W \cdot m^{-1} \cdot K^{-1}$ at room temperature,[32] and penta-$PdTe_2$ and penta-$PtTe_2$ have low thermal conductivities of 1.42^{33} and 1.77 $W \cdot m^{-1} \cdot K^{-1}$,[34] respectively. Therefore, it can be expected that the penta-OsP_2 and penta-RhS_2 sheets cleaved from marcasite and pyrite phases could possess low lattice thermal conductivity due to their pentagonal configurations and containing heavy transition elements, which is beneficial for thermoelectric applications, which are different from the reported systems with high thermoelectric performance like nano-defected bulk BiSbTe/amorphous boron composites,[35] and fiber-based[36] and grain boundary-engineered systems.[37]

In this work, we identify two new semiconducting pentagon-based 2D materials, penta-OsP_2 and penta-RhS_2. Based on state-of-the-art first-principles calculations, we study their dynamical, thermal, and mechanical stability, and show that they both possess low lattice thermal conductivity with potential thermoelectric applications. We also compare their thermal transport properties with those of penta-PdS_2, as penta-RhS_2 and penta-PdS_2 are both pentagon-based group VIII metal sulfides.

2. Computational methods

Our calculations within the scheme of density functional theory are performed by using the Vienna ab initio simulation package (VASP),[38,39] where the projected augmented wave method[40] is used for describing the interactions between the valence electrons and ions. The exchange-correlation interaction among the electrons is treated by using the generalized gradient approximation[41] with the Perdew-Burke-Ernzerhof (PBE) functional[42] in geometry optimization and properties calculations. The Heyd-Scuseria-Ernzerhof (HSE06) hybrid functional[43,44] is used for calculating the electronic structures. The wavefunctions of valence electrons are expanded by plane waves with energies up to 600 eV. The vacuum space with a thickness of 13 Å is set in these systems to avoid the fake interactions between periodic images. The first Brillouin zone is sampled by a k mesh with the grid density of $\sim 2\pi \times 0.02$ Å^{-1}, namely, $11\times13\times1$, $13\times13\times1$ and $11\times9\times1$ for the primitive cells of penta-OsP$_2$, penta-RhS$_2$ and penta-PdS$_2$ respectively. The criteria for the convergence of energy in self-consistent field iterations and interatomic forces are set to 10^{-7} eV and 10^{-5} eV·Å^{-1}, respectively. Ab initio molecular dynamic (AIMD) simulations for these systems are performed under the canonical NVT ensemble with the Nosé-Hoover thermostat.[45] The Seebeck coefficient and the electrical conductivity are calculated using the BoltzTrap2 software.[46]

The intrinsic lattice thermal conductivity κ_L is calculated by solving linearized phonon Boltzmann transport equation (BTE),[47] as implemented in the ShengBTE code,[48] which can be expressed by the equation

$$\kappa_{\text{L}}^{\alpha\beta} = \frac{1}{k_{\text{B}}T^2\Omega N}\sum_{\lambda} f_0\left(f_0+1\right)\left(\hbar\omega_\lambda\right)^2 v_\lambda^\alpha F_\lambda^\beta , \qquad (1)$$

where $\lambda = (\boldsymbol{q}, j)$ denotes the jth phonon mode at coordinate $\boldsymbol{q}$ in the first Brillouin zone, ω_λ, Ω, N, f_0, v_λ^α and F_λ^β are the phonon frequency, the volume of the primitive cell, the number of uniform $\boldsymbol{q}$ points, the Bose-Einstein distribution, the group velocity and the mean free path, respectively, and α/β indicates the Cartesian direction x or y. The 2nd-order and 3rd-order interatomic force constants (IFCs), as inputs to the BTE for calculating ω_λ, v_λ^α and F_λ^β, are obtained by using Phonopy[49] and the HiPhive package,[50] respectively. A total number of 200 rattled $3\times4\times1$ and $4\times4\times1$ supercells of penta-RhS$_2$ and penta-OsP$_2$, and 60 rattled $4\times4\times1$ supercells of penta-PdS$_2$ are respectively generated to calculate the interatomic forces for the least-squares fitting of 3rd-order IFCs with the cutoff radius of 6.0 Å, guaranteeing a sufficient ratio (over 6:1) between the target values and the nonzero parameters. The detailed parameters and goodness of fit are summarized in Table S1 in the ESI. The random displacements are generated by a rattle procedure with a standard deviation of 0.01 Å for penta-OsP$_2$ and penta-PdS$_2$, and 0.02 Å for penta-RhS$_2$. 1% of the raw data are used as the test set during the fitting process. The BTE is solved with a $61\times61\times1$ $\boldsymbol{q}$-mesh for penta-OsP$_2$, and with a $51\times51\times1$ $\boldsymbol{q}$-mesh for penta-RhS$_2$ and penta-PdS$_2$.

3. Results and discussions

3.1 Geometry and stability

The bulk marcasite and pyrite structures, as shown in Fig. 1(a$_1$) and (b$_1$), are both

in the chemical formula of MA_2, and are the parent materials for pentagon-based sheets penta-MS_2 (M = Mn, Ni, Cu/Ag and Zn/Cd),[31] because they contain internal pentagonal configurations, which could lead to the top-down synthesis of 2D pentagon-based materials. A typical example is the liquid-phase exfoliation of iron pyrite for penta-FeS_2 sheets.[27,28] However, the corresponding marcasite and pyrite counterparts of many predicted pentagon-based sheets do not exist. Thus, we start the search from the experimentally identified marcasite and pyrite materials listed in Materials Project.[51] Here, we don't adopt the optimized geometries of the directly cleaved sheets like previous studies,[29,31] because their energies increase during the exfoliation of bulk materials[2] and the energy difference between the two pentagon-based configurations with same chemical formula[31] tend to be in the same order of magnitude (0.1 eV/atom), indicating that the phase transition can be triggered during the chemical exfoliation. A similar phenomenon was found in the famous transition-metal dichalcogenide MoS_2, where its 1T-, 1T'- and 2H-phases coexist in the chemically exfoliated sheet.[52] Instead, we rationally construct the typical penta-CN_2[53] and penta-$PdSe_2$[22] configurations with the chemical formula of the bulk counterparts as the initial conjectures for geometry optimizations, so that the possible phase transitions can be properly treated. For each configuration, we check its dynamical stability and electronic band structure to identify the stable semiconducting pentagon-based sheets with low lattice thermal conductivity.
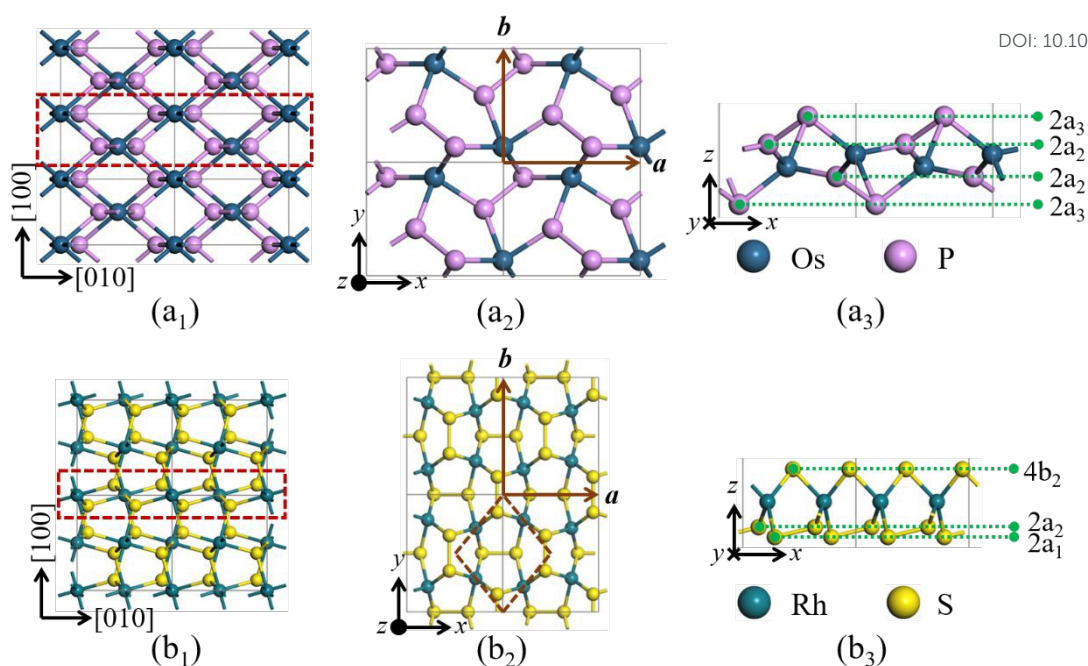
Fig. 1 (a_1, b_1) Bulk phase of marcasite and pyrite. Dashed red rectangles highlight the embedded pentagon-based 2D frameworks. (a_2, b_2) Top and (a_3, b_3) side views of the cleaved penta-OsP_2 and penta-RhS_2 sheets. Dashed brown rhombus indicates a primitive cell of penta-RhS_2.

From the exfoliated sheets of all the marcasite and pyrite materials, we find that the dynamically stable semiconducting pentagon-based sheet with the heaviest average atomic mass is the 2D OsP_2 system from the marcasite-phase OsP_2, as shown in Fig. 1(a_2) and (a_3). The optimized structure possesses a monoclinic unit cell with a space group symmetry $P2_1$ (No. 4) with the lattice parameters a = 5.22 Å, b = 4.33 Å and γ = 90°, and each unit cell contains two Os atoms and four P atoms. The four-fold coordinated Os atoms in penta-OsP_2 occupy the Wyckoff position $2a_1$ (0.004, 0.866, 0.515), while the three-fold coordinated P atoms occupy two nonequivalent Wyckoff positions $2a_2$ (0.641, 0.586, 0.538) and $2a_3$ (0.354, 0.865, 0.603), leading to the buckled structure with a buckling height of 3.24 Å. Each P atom on the outer-most $2a_3$ site of

the 2D sheet is bonded to a P atom on the inner $2a_2$ site, forming a tilted P_2 dimer.

To study the dynamical stability of penta-OsP_2, we calculate its phonon band structure via the finite displacement method implemented in Phonopy.[49] As shown by the blue lines in Fig. 2(a), no any imaginary phonon modes are found in the entire first Brillouin zone, confirming that penta-OsP_2 is dynamically stable. For comparison, the phonon band structure obtained by HiPhive[50] is also plotted by the greenish scatter points, which coincides well with the result from Phonopy, adding to the credibility of IFCs from the fitting process. It is interesting to note that the monoclinic symmetry of penta-OsP_2 is for the first time found in a binary pentagon-based sheet, although it has been found in penta-silicene,[54] and some ternary pentagon-based sheets, for example, penta-$FeAsS$,[55] penta-BCN,[15] and penta-CNP.[17]

As to the pentagon-based configurations with imaginary phonon modes, we manage to identify the fully relaxed geometry based on the eigenvectors of the imaginary phonon modes, because they point toward the decline in total energy on the potential surface. Take the pentagon-based 2D RhS_2 system cleaved out of the pyrite-phase RhS_2 as an example. The phonon band structures of the optimized geometries of RhS_2 with the penta-CN_2 and penta-$PdSe_2$ configurations both possess imaginary phonon modes, and the former possesses five imaginary optical phonon branches, which all feature the distortion of its tetrahedral symmetry and the Rh-S tetrahedrons. The details are shown in Fig. S1 in the ESI. Thus, we rationally construct a new initial conjecture with a reduced symmetry by breaking the tetragonal symmetry of RhS_2 with a shear strain. As illustrated in Fig. 1(b_2) and (b_3), the optimized geometry of the sheared

RhS$_2$ lattice remains pentagon-based, and it turns into a monoclinic Cm (space group no. 8) symmetry. Thus, the structure is termed penta-RhS$_2$. The unit cell of penta-RhS$_2$ possesses the lattice parameters a = 5.66 Å, b = 6.92 Å and γ = 90°, and contains four Rh atoms and eight S atoms. The Rh atoms occupy the Wyckoff position 4b$_1$ (0.283, 0.283, 0.710), and, similar to the complex chemical environment of P atoms in penta-OsP$_2$, the S atoms occupy three nonequivalent Wyckoff positions, namely, 2a$_1$ (0.218, 0.0, 0.818), 2a$_2$ (0.361, 0.0, 0.788), and 4b$_2$ (0.056, 0.849, 0.611). Each S atom on the 2a$_1$ site forms a tilted S$_2$ dimer with an S atom on the 2a$_2$ site, and the S atoms on the 4b$_2$ site form a horizontal S$_2$ dimer with one another, leading to a Janus configuration with different upper and lower surfaces and a finite buckling height of 3.40 Å. We calculate the phonon band structure via Phonopy[49] and HiPhive,[50] and find no any imaginary phonon modes from both approaches, as shown in Fig. 2(b). To our best knowledge, this pentagon-based configuration of penta-RhS$_2$ with the Cm symmetry and a Janus configuration is the first of its kind.
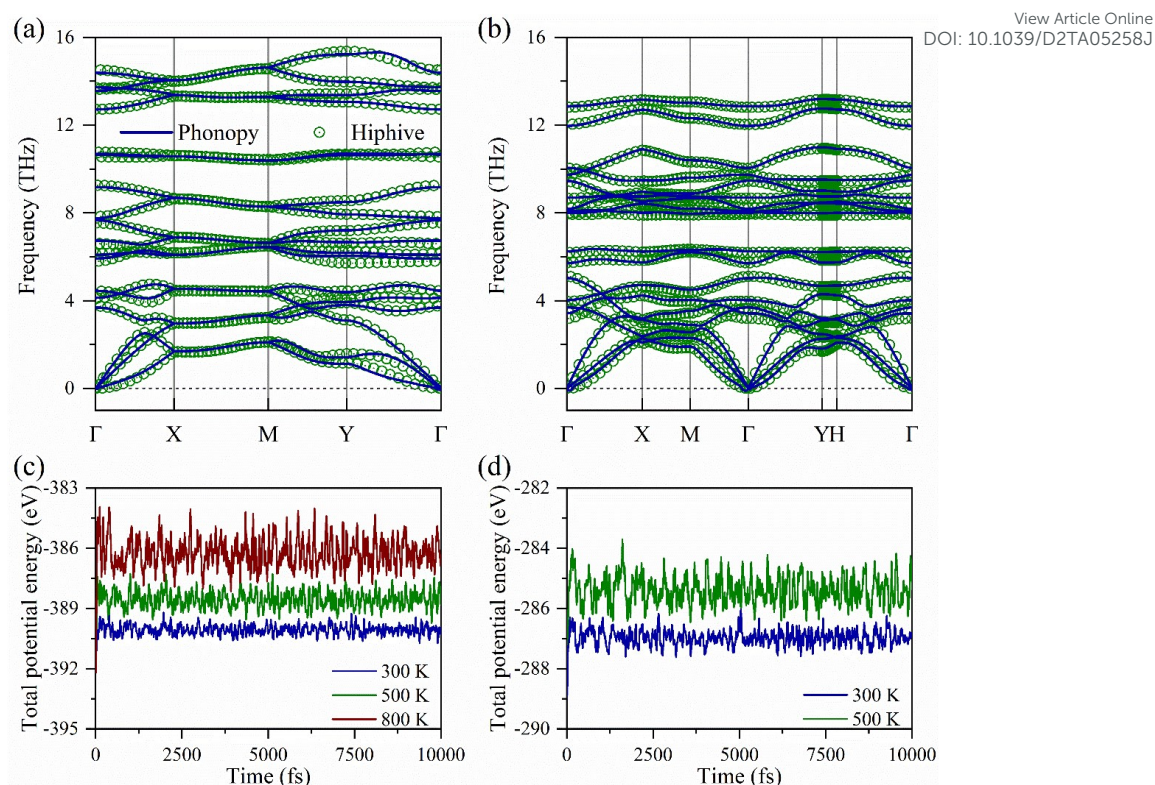
Fig. 2 Phonon band structure of (a) penta-OsP$_2$ and (b) penta-RhS$_2$. Total potential energy fluctuation in (c) penta-OsP$_2$ and (d) penta-RhS$_2$ during AIMD simulations at different temperatures.

In addition to their dynamical stability, we also check the thermal and mechanical stabilities of the two new pentagon-based structures. We examine the thermal stability of the two structures by performing AIMD simulations at different temperatures for 10 ps with a time step of 1 fs. The 3×3 supercells of penta-OsP$_2$ and penta-RhS$_2$ are used to avoid the fake stability caused by the periodic boundary conditions. As shown in Fig. 2(c), the total potential energies of penta-OsP$_2$ during the simulations at 300, 500, and 800 K all vibrate around constant levels, and the geometries of the supercells after these simulations remain intact, indicating that penta-OsP$_2$ is thermally stable at temperatures up to 800 K. While for penta-RhS$_2$, its total potential energies vibrate around constant levels throughout the simulations at 300 and 500 K, as shown in Fig. 2(d). However,

the energy level drifts during the simulation at temperatures beyond 500 K, indicating that penta-RhS$_2$ can withstand temperature up to 500 K. To rule out the unreasonable size effect on phonon of the system at finite temperature, we also perform an AIMD simulation under the NPT ensemble at 600 K to obtain the correct lattice parameters for the successive NVT simulation, which confirms the instability of penta-RhS$_2$ at this temperature. More details can be found in Text S1 and Fig. S2 in the ESI.

We then evaluate the mechanical stability of these structures based on their stiffness tensor components C_{11}, C_{22}, C_{66}, and C_{12} under Voigt notation.[56] As shown in Table 1, the stiffness tensor components of both penta-OsP$_2$ and penta-RhS$_2$ fully satisfy the Born-Huang criteria[57] for mechanical stability, namely, $C_{ii} > 0$ ($i = 1, 2$ and 6) and $C_{11} \cdot C_{22} > C_{12}^2$ for the 2D structures with the lattice parameter $\gamma = 90°$. We also calculate the linear mechanical properties of the two structures, and find that the stiffness of penta-OsP$_2$ possesses large anisotropy along the two axial directions, with its Young's modulus along the x axis about three times larger than that along the y axis. While, the Young's moduli of penta-RhS$_2$ along the two directions are slightly different by 5% despite of its nonequivalent x and y directions due to monoclinic symmetry. In addition, by dividing the Young's modulus of a 2D material (in GPa·nm) with its thickness (the sum of its buckling height and a van der Waals distance of 3.40 Å), we can get the effective Young's modulus E^{eff} (in GPa) for comparison with the Young's modulus of bulk materials. It is found that the E^{eff} of penta-OsP$_2$ (143.01 GPa along x axis, and 43.89 GPa along y axis) is much lower than the Young's modulus of marcasite-phase OsP$_2$ (ranging from 290.8~538.4 GPa along different directions).[58] It

is also worth noting that penta-OsP$_2$ possesses a significant negative Poisson's ratio of −0.24 along the diagonal direction, which is not found in marcasite-phase OsP$_2$.[58] It is worthy to note that the electronic properties of a system with NPR would change significantly under external stress due to the variation of the orbital interactions of atoms induced by the changes of the bond lengths and bond angles, as demonstrated in multilayer graphene.[59] More discussions on the mechanical properties of the two structures are presented in Text S2 and Fig. S3 in the ESI.

Table 1 Stiffness tensor components C_{11}, C_{22}, C_{12}, and C_{66} (in GPa·nm), Young's modulus E_x and E_y (in GPa·nm), and Poisson's ratio v_x and v_y of penta-OsP$_2$ and penta-RhS$_2$.

Structure	C_{11}	C_{22}	C_{12}	C_{66}	E_x	E_y	v_x	v_y
penta-OsP$_2$	105.22	32.29	18.20	47.86	94.96	29.14	0.56	0.17
penta-RhS$_2$	67.70	64.15	12.72	9.61	65.18	61.76	0.20	0.19

3.2 Electronic structure

We calculate the electronic structures of penta-OsP$_2$ and penta-RhS$_2$ at the HSE06 level. The first Brillouin zones of the unit cell of penta-OsP$_2$ and the primitive cell of penta-RhS$_2$, as shown in Fig. S4 in the ESI, are represented by the high-symmetry paths Γ (0.0, 0.0)→ X (0.5, 0.0)→ M (0.5, 0.5)→ Y (0.0, 0.5)→ Γ and Γ (0.0, 0.0)→ X (0.418, 0.418)→ M (0.0, 0.5)→ Γ→ Y (−0.5, 0.5)→ H (−0.418, 0.582)→ Γ, respectively. As shown in the electronic band structures in Fig. 3(a) and 3(b), the two pentagon-based structures are both semiconductors. Penta-OsP$_2$ possesses an indirect band gap of 0.78 eV, whose valence band maximum (VBM) and conduction band minimum (CBM) are

located at the high-symmetry points Γ and Y, respectively. It is also worth mentioning that the band gap of penta-OsP_2 at the PBE level (0.44 eV) is lower than that (0.92 eV) of marcasite-phase OsP_2.[58] This is because the energy level broadening that usually happens during the increase in dimensionality is overwhelmed by the changes in electronic states due to the changes in the geometry of OsP_2. While, penta-RhS_2 has a direct band gap of 0.93 eV at the high-symmetry point Γ. The band gaps of both the two pentagonal sheets are smaller than that of the synthesized penta-$PdSe_2$ ($\sim$1.3)[22] and penta-NiN_2 ($\sim$1.1 eV),[26] which have been found to be desired for thermoelectric applications. By analyzing the projected DOS (PDOS) of penta-OsP_2 and penta-RhS_2, it is found that electron states near the Fermi levels of both pentagon-based sheets are mutually contributed by the corresponding transition-metal atoms and the P_2/S_2 dimers. The above results are double-checked by taking the spin polarization into consideration, and the local magnetic moments in the resulting electronic structures remain zero, indicating that both penta-OsP_2 and penta-RhS_2 are indeed nonferromagnetic.

To better understand the nature of the tilted dimers in penta-OsP_2 and penta-RhS_2, we study their deformation charge density. As shown in Fig. 3(c), the outer-most P atom on the $2a_3$ site of penta-OsP_2 gains electrons from the inner $2a_2$-P atom, where the gained electrons distribute along the out-of-plane direction. Such charge transfer is confirmed by the Bader charge analysis[60] where each P atom on site $2a_3$ possesses 0.04 more electrons than the $2a_2$-P atom. Detailed results on the Bader charge distribution are concluded in Table S2 in the ESI. This can be understood as the preference of the lone-pair electrons on a single P atom over the π bond between the parallel p_z orbitals

of adjacent P atoms. Such phenomenon is previously reported in the penta-silicene with the same geometry.[54] Similarly, a charge accumulation is found on the outer-most $2a_1$-S atom in the tilted S_2 dimer, where each $2a_1$-S atom possesses 0.06 more electrons than the adjacent $2a_2$-S atom, though it is not apparent qualitatively in Fig. 3(d). The polarized dimers in penta-OsP$_2$ and penta-RhS$_2$ naturally lead to finite spontaneous in-plane electric polarizations of 0.70 and 0.67 $e\cdot\text{Å}$ per primitive cell along their x axes, respectively. Meanwhile, the polarization between the different S_2 dimers on both sides of the Janus penta-RhS$_2$ configuration further contributes to a tremendous out-of-plane electric dipole of 12.61 $e\cdot\text{Å}$ per primitive cell.
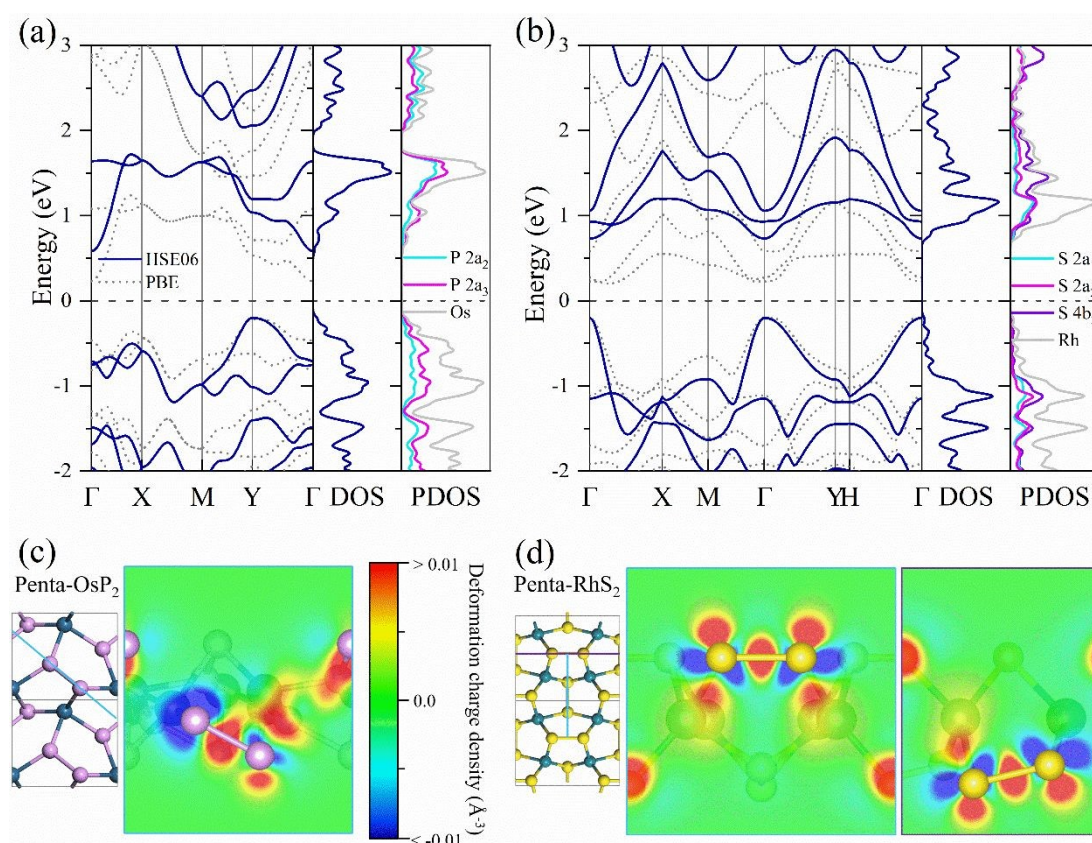

Fig. 3 (a, b) Electronic band structure, total DOS and PDOS of penta-OsP$_2$ and penta-RhS$_2$, respectively. (c, d) Deformation charge density around the P$_2$ dimers in penta-

OsP$_2$ and the S$_2$ dimers in penta-RhS$_2$.

We also calculate the carrier mobilities of penta-OsP$_2$ and penta-RhS$_2$ based on deformation potential theory. A modified version of the Bardeen-Shockley equation deduced by Lang et al.[61] is used to account for the significant anisotropy in these structures, where the combinations of the parameters from both x and y directions are introduced as the overall contribution from phonons propagating along the two axial directions. For example, the carrier mobility μ_x along the x direction is determined by the stiffness tensor components (C_{11} and C_{22}), the effective mass (m_x^* and m_y^*), and the deformation potential ($E_{1,x}$ and $E_{1,y}$) along both axial directions, as shown in equation 2.

$$\mu_x = \frac{e\mathsf{h}^3\left(\dfrac{5C_{11}+3C_{22}}{8}\right)}{k_B T \left(m_x^*\right)^{\frac{3}{2}}\left(m_y^*\right)^{\frac{1}{2}}\left(\dfrac{9E_{1,x}^2+7E_{1,x}E_{1,y}+4E_{1,y}^2}{20}\right)} \tag{2}$$

The calculated results are summarized in Table S3. It is found that, penta-OsP$_2$ possesses a significant electron mobility (1857.09 cm$^2\cdot$V$^{-1}\cdot$s^{-1} along the x direction) due to its low deformation potential and low electron effective mass, and penta-RhS$_2$ exhibits a relatively high hole mobility (180.55 cm$^2\cdot$V$^{-1}\cdot$s^{-1} along the y direction) due to its low hole effective mass along that direction. For comparison, the electron and hole mobilities of penta-PdS$_2$ are lower than 100 cm$^2\cdot$V$^{-1}\cdot$s^{-1}.

3.3 Lattice thermal conductivity

Next, we evaluate the lattice thermal conductivity of penta-OsP$_2$ and penta-RhS$_2$

at different temperatures by solving BTE. For comparison, the lattice thermal

conductivity of penta-PdS$_2$[33,62] is also calculated. (See Fig. S5 in the ESI for details on

the geometry and phonon/electronic band structure of penta-PdS$_2$.) The 3rd-order IFCs

as raw data for iteratively solving BTE is obtained with the HiPhive package.[50] The

calculated lattice thermal conductivities κ_L are shown in Fig. 4(a$_1$)-(a$_3$). The κ_L of penta-

OsP$_2$, penta-RhS$_2$ and penta-PdS$_2$ along the x/y direction is 14.46/3.19, 2.90/3.20, and

17.17/29.90 W·m^{-1}·K^{-1} at 300 K, respectively, and each (κ_L, T) data set fits well with

the $\kappa_L \propto T^{-1}$ relationship. The values of κ_L for both penta-OsP$_2$ and penta-RhS$_2$ are

lower than that of penta-PdS$_2$. The former is partially attributed to the heavier atomic

mass of Os over Pd, while the latter is because of to its intriguing low-symmetry
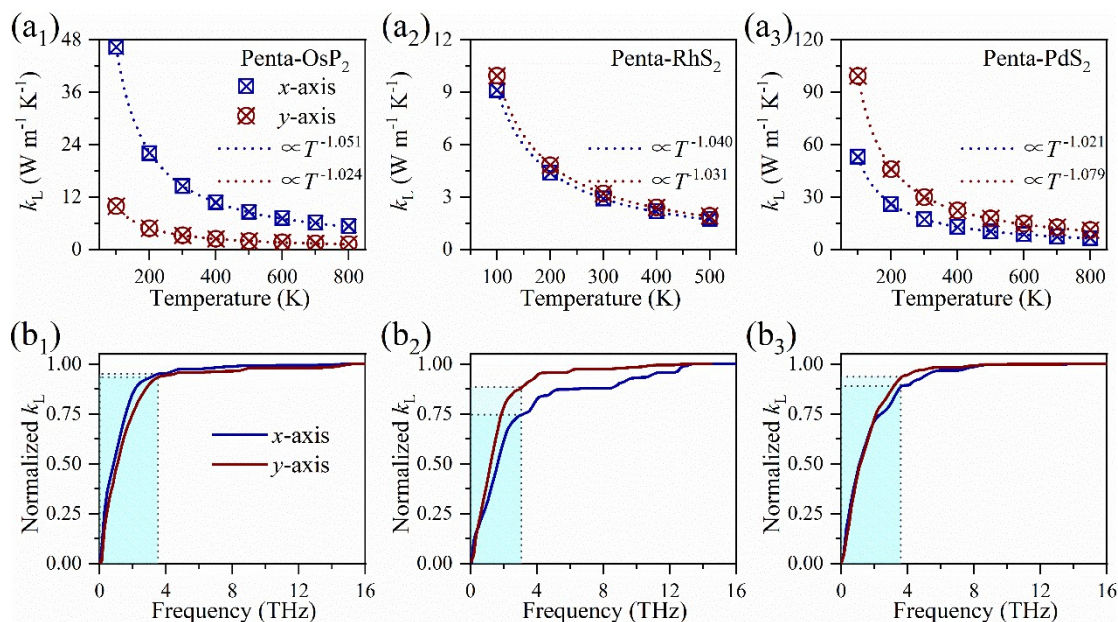
pentagon-based geometry.

Fig. 4 (a$_1$, a$_2$, a$_3$) Lattice thermal conductivity κ_L of penta-OsP$_2$, penta-RhS$_2$, and penta-PdS$_2$ as function of temperature. (b$_1$, b$_2$, b$_3$) Variation of the normalized cumulative κ_L of penta-OsP$_2$, penta-RhS$_2$, and penta-PdS$_2$ at 300 K with phonon frequency.

In addition, in the calculated normalized cumulative κ_L at 300 K, as shown in Fig. 4(b_1)-(b_3), the acoustic phonon modes of penta-OsP$_2$, penta-RhS$_2$, and penta-PdS$_2$ contribute up to 95%/93%, 75%/88%, and 89%/94% of their lattice thermal conductivities along the x/y direction, respectively. In these three cases, the direction in which acoustic phonon modes contribute more coincides with the direction with a larger κ_L, i.e., the x direction for penta-OsP$_2$ and y direction for penta-RhS$_2$ and penta-PdS$_2$.

3.4 Harmonicity and anharmonicity

Then, we explore the origin of the low lattice thermal conductivities of penta-OsP$_2$ and penta-RhS$_2$ as compared to that of penta-PdS$_2$ by analyzing their harmonicity and anharmonicity. The harmonicity of a crystalline material is usually represented by its phonon group velocity and three-phonon (P$_3$) phase space, which can be calculated from the 2nd-order IFCs alone. The weighted P$_3$ phase space (WP$_3$) of penta-OsP$_2$, penta-RhS$_2$ and penta-PdS$_2$ are comparable in the magnitude of 10^{-7}, as shown in Fig. 5(a_1)-(a_3). However, the group velocities (v_g) of these three pentagon-based sheets, as presented in Fig. 5(b_1)-(b_3), show a difference, where the maximum v_g of the acoustic phonon modes in penta-PdS$_2$ (6.49 km/s) prevails over that in both penta-OsP$_2$ (5.64 km/s) and penta-RhS$_2$ (4.68 km/s). The low v_g partially accounts for the reduction of the thermal conductivity of penta-OsP$_2$ and penta-RhS$_2$.
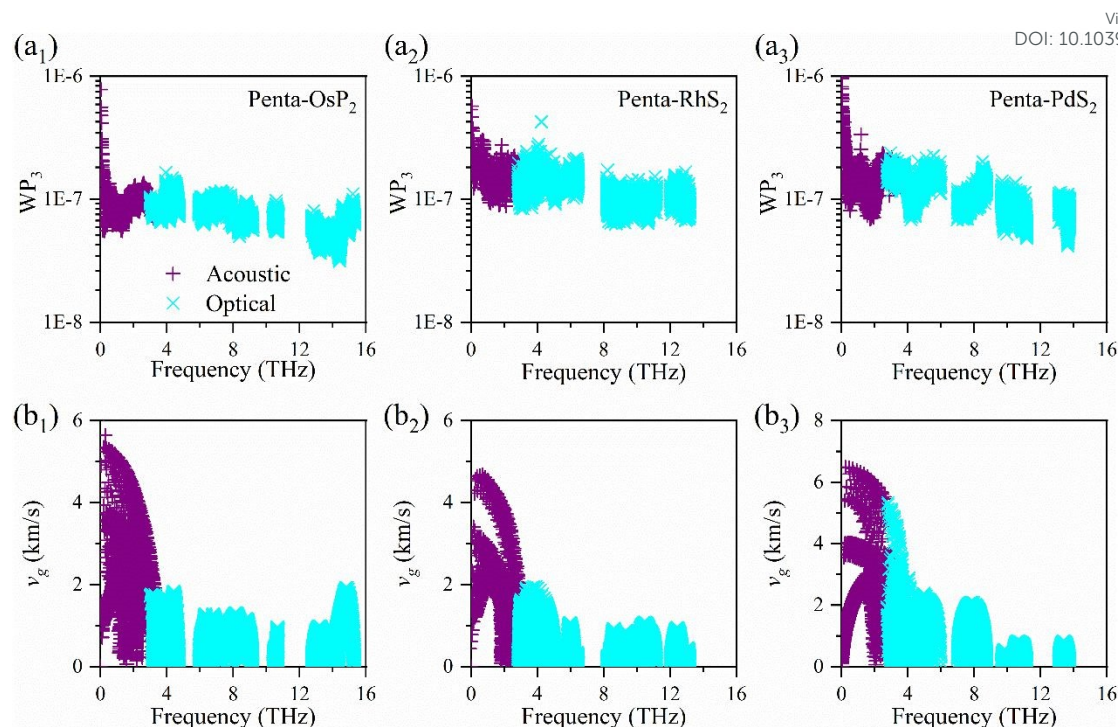
Fig. 5 (a_1, a_2, a_3) Weighted P_3 phase space WP_3, and (b_1, b_2, b_3) group velocity v_g of penta-OsP$_2$, penta-RhS$_2$, and penta-PdS$_2$.

Then, we evaluate the anharmonicity of penta-OsP$_2$, penta-RhS$_2$ and penta-PdS$_2$, which is usually described by the Grüneisen parameter and the three-phonon scattering rate, and is further visualized by the trajectory of ions during AIMD simulations. We first calculate the Grüneisen parameter of the three structures, which is defined by the change in phonon frequency with respect to the volume of the primitive cell. As shown in Fig. 6(a_1)-(a_3), the Grüneisen parameters of the out-of-plane flexural acoustic phonon modes (also known as the ZA mode) of the three pentagon-based sheets have large negative values at the zero-frequency limit, as is the case in all 2D structures.[63] While, the Grüneisen parameters of the other phonon modes in these structures fall in the range of [−2, 2], and are comparable to one another. We then calculate the three-phonon scattering rates ω of penta-OsP$_2$, penta-RhS$_2$, and penta-PdS$_2$, which are further

resolved to the normal scattering process (N-process) with conserved lattice momentum
and the umklapp scattering process (U-process) where the lattice momenta before and
after the scattering diverge by the lattice vectors of the reciprocal space. The results are
plotted in Fig. 6(b_1)-(b_3). For reference, the overall scattering rate is given in Fig. S6 in
the ESI. It is found that the scattering rate of the acoustic phonons penta-RhS$_2$ is in
general larger than that in penta-PdS$_2$, whereas that in penta-OsP$_2$ is comparable with
that in penta-PdS$_2$. And it is found that the scattering rate of penta-RhS$_2$ is mostly
contributed by the U-processes. The strong U-process scattering in penta-RhS$_2$
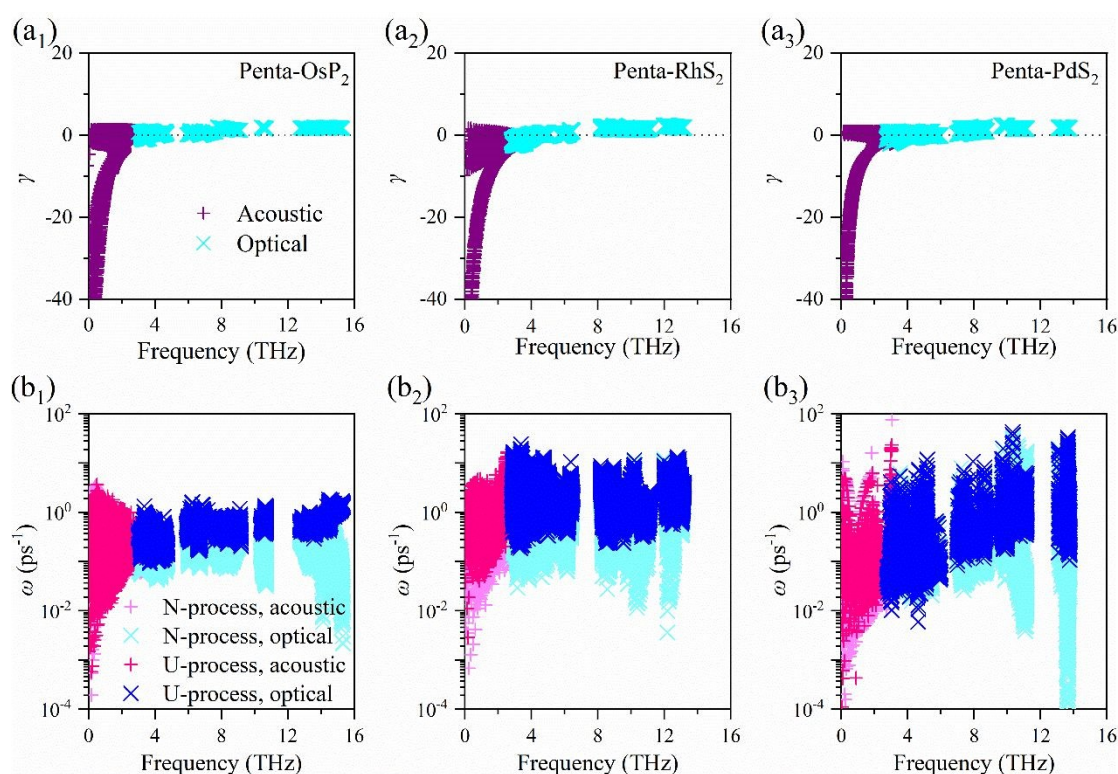contributes to its low κ_L in addition to its low acoustic v_g.

Fig. 6 (a_1, a_2, a_3) Grüneisen parameter γ, and (b_1, b_2, b_3) scattering-process resolved
scattering rate ω of penta-OsP$_2$, penta-RhS$_2$, and penta-PdS$_2$.

We visualize the anharmonicity of the pentagon-based 2D structures by plotting the trajectory of their atoms during the AIMD simulations at 300 K in Fig. S7. We also calculate the mean square displacements (MSD) of the three systems based on the statistical analysis of these trajectories. The results are summarized in Table 2. While the MSDs and the trajectories of the three pentagon-based 2D structures all show anisotropy between the in-plane and out-of-plane rattling, differences in their anharmonicity are evident. The trajectory and the MSD of the Os and P atoms in penta-OsP_2 and the S atoms in penta-RhS_2 all show considerable anisotropy along the x and y axes. Namely, the vibration of Os and P atoms along the y axis in penta-OsP_2 is stronger, and that of S atoms along the x axis in penta-RhS_2 is stronger, which are signs of strong anharmonicity in both systems. In contrast, the MSD of Pd and S atoms in penta-PdS_2 along the x and y axes are comparable, and their trajectories are also isotropic with a round dispersion around the equilibrium position, both indicating strong harmonicity in penta-PdS_2. And large differences in MSD are found in between both the nonequivalent P atoms in penta-OsP_2 (up to 61%) and the nonequivalent S atoms in penta-RhS_2 (up to 39%). Thus, it is implied that the large MSD and the deviation between MSDs of atoms of the same element both coincide with low κ_L. A similar phenomenon is found in the previous work.[64]

Table 2 MSD (in Å) along three axial directions of the atoms at nonequivalent Wyckoff positions in penta-OsP$_2$, penta-RhS$_2$, and penta-PdS$_2$ during AIMD simulations at 300 K.

penta-OsP$_2$		penta-RhS$_2$		penta-PdS$_2$	
Atom	MSD	Atom	MSD	Atom	MSD
2a$_1$ Os	(0.047, 0.061, 0.134)	4b$_1$ Rh	(0.071, 0.079, 0.112)	2b Pd	(0.059, 0.059, 0.194)
2a$_2$ P	(0.062, 0.071, 0.132)	4b$_2$ S	(0.092, 0.099, 0.106)	4e S	(0.079, 0.073, 0.205)
2a$_3$ P	(0.093, 0.114, 0.117)	2a$_1$ S	(0.128, 0.103, 0.109)		
		2a$_2$ S	(0.118, 0.084, 0.117)		

3.5 Thermoelectric performance

Based on the results obtained above, we further calculate the thermoelectric properties of penta-OsP$_2$ and penta-RhS$_2$. The thermoelectric performance is usually evaluated by a dimensionless figure of merit $ZT = S^2\sigma T/(\kappa_e + \kappa_L)$, where S, σ, κ_e, and κ_L are the Seebeck coefficient, electrical conductivity, electronic thermal conductivity, and lattice thermal conductivity, respectively. Here, κ_e is calculated from σ based on Wiedemann-Franz law ($\kappa_e = L\sigma T$), where the Lorenz number $L = 1.5 \times 10^{-8}$ W·Ω·K^{-2} is treated as a system-independent constant,[65] which has been commonly used in previous studies for describing the thermal transport of electronic states with high Seebeck coefficient.[66,67] A high ZT value would lead to a high thermoelectric conversion efficiency. Due to their high carrier mobilities and low lattice thermal conductivities, penta-OsP$_2$ and penta-RhS$_2$ could possess significant thermoelectric responses. Because it is challenging to develop materials with high ZT values operating in 300~500 K, we evaluate the thermoelectric properties at 500 K. The calculated Seebeck

coefficient S, electrical conductivity σ, and electronic thermal conductivity κ_e are presented in Fig. 7, as a function of the chemical potential μ, respectively. Their corresponding ZT values are plotted in Fig. 8. The ZT values of penta-OsP$_2$ and penta-RhS$_2$ both show strong anisotropy due to their highly anisotropic electric conductivities and electronic thermal conductivities. The optimized ZT value for p-type penta-OsP$_2$ is found to be 1.21 along the y direction at the hole-doping concentration of 5.51×10^{13} cm^{-2}, while for n-type penta-OsP$_2$, the ZT value is 1.18 along the x direction at the electron-doping concentration of 5.75×10^{12} cm^{-2}, indicating that thermoelectric devices based on p-type and n-type penta-OsP$_2$ sheets should have comparable conversion efficiencies. The large electrical conductivity in n-type penta-OsP$_2$ does not contribute to a higher optimized ZT value, because κ_e in both p-type and n-type sheets is larger than κ_L, as shown in Fig. 7(c$_1$), and thus, according to Wiedemann-Franz law ($\kappa_e = L\sigma T$), the electrical conductivity term and the electronic thermal conductivity term cancel out when κ_L can be neglected, leading to an approximation of $ZT \approx S^2/L$. Meanwhile, p-type penta-RhS$_2$ possesses an optimized ZT value of 1.33 at the hole-doping concentration of 6.43×10^{12} cm^{-2}. For a similar reason [$\kappa_e > \kappa_L$, as shown in Fig. 7(c$_2$)], the optimized ZT value of p-type penta-RhS$_2$ is slightly higher than that of penta-OsP$_2$, even though penta-RhS$_2$ possesses a lower carrier mobility. The relatively larger ZT value of penta-RhS$_2$ can be attributed to its smaller band gap for better exploiting the peak Seebeck coefficient values near $\mu = 0$ eV. In contrast, penta-PdS$_2$ possesses weakly anisotropic thermoelectric responses, and its optimized ZT values ($\sim$0.1) are much lower, because it possesses much larger κ_L and band gap values.
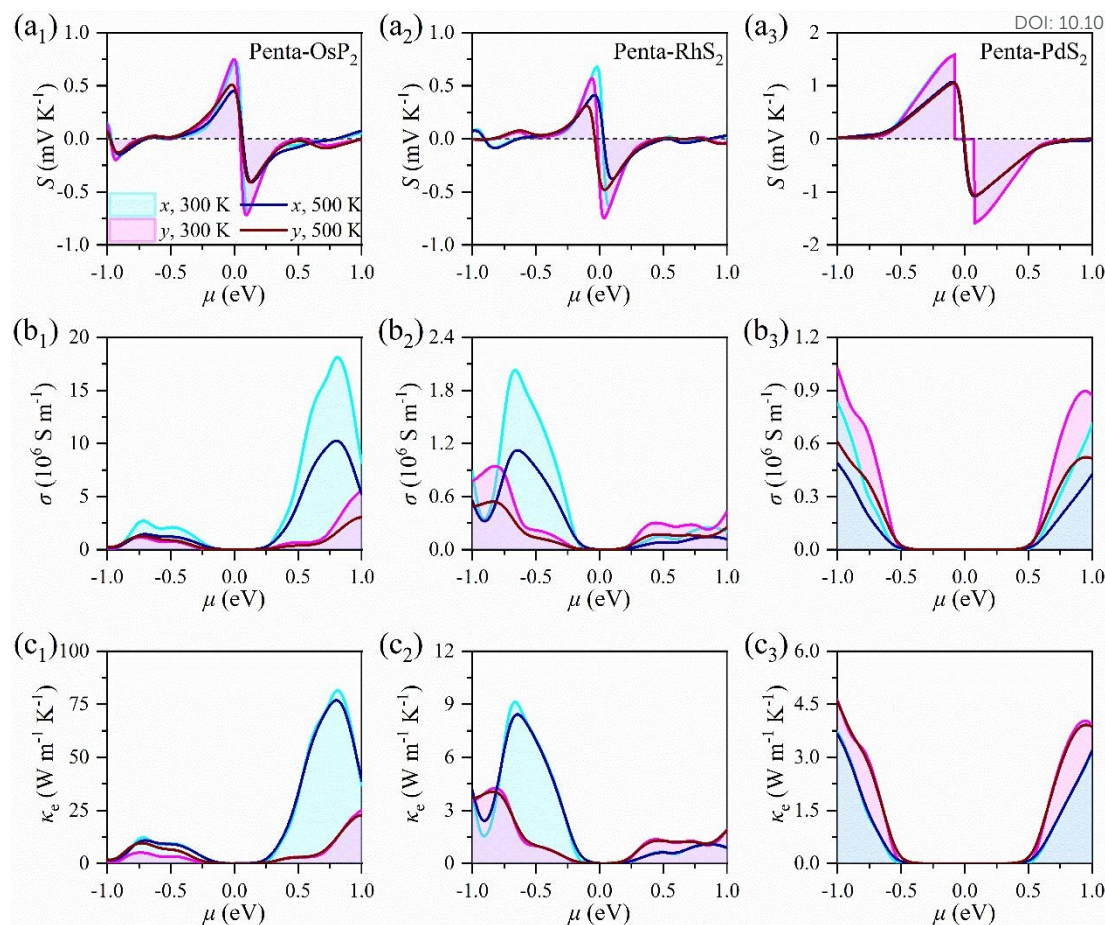
Fig. 7 (a_1, a_2, a_3) Variation of Seebeck coefficient S, (b_1, b_2, b_3) electrical conductivity σ, and (c_1, c_2, c_3) electronic thermal conductivity κ_e with the chemical potential μ for penta-OsP$_2$, penta-RhS$_2$, and penta-PdS$_2$, respectively.
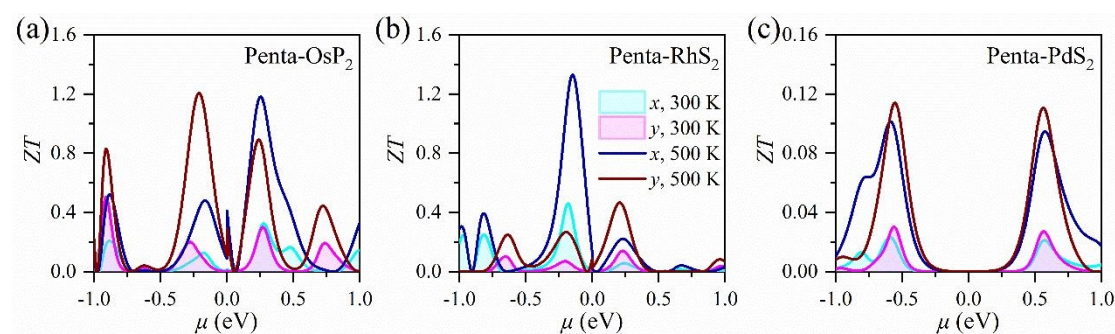
Fig. 8 Change of the ZT value with the chemical potential μ for (a) penta-OsP$_2$, (b) penta-RhS$_2$, and (c) penta-PdS$_2$.

4. Conclusions

Materials with low thermal conductivity and high thermoelectric performance are of current interest. Among them, pentagon-based structures provide the unique platform, where the intrinsic stress induced by pentagonal units endows the systems with intrinsically high anharmonic phonon scattering, resulting in low lattice thermal conductivity. This special feature stimulates the efforts on seeking and designing new pentagon-based materials. In this work, by theoretically cleaving thin layers with few-atom thickness from the existing bulk marcasite and pyrite structures, we have identified two new semiconducting pentagon-based 2D structures, penta-OsP_2 and penta-RhS_2, and found that both of them possess thermal, dynamical, and mechanical stability, and exhibit high carrier mobilities. More interestingly, these new binary pentagon-based sheets have weak harmonicity and strong anharmonicity, and exhibit low lattice thermal conductivity of 3.19 and 2.90 $W \cdot m^{-1} \cdot K^{-1}$ at room temperature, respectively, which is about an order of magnitude lower than that of the synthesized penta-PdS_2 sheet. The high mobility and the low lattice thermal conductivities make penta-OsP_2 and penta-RhS_2 promising candidates for thermoelectric applications with optimized ZT values of 1.2~1.3 at 500 K. Our work expands the family of pentagon-based structures with intriguing features, which would stimulate experimental efforts to synthesize pentagon-based structures by chemical exfoliation as theoretically suggested in this work.

Journal of Materials Chemistry A Accepted Manuscript

Acknowledgments

Conflicts of interest

There are no conflicts of interest to declare.

References

1. S. Zhang, J. Zhou, Q. Wang, X. Chen, Y. Kawazoe and P. Jena, Penta-graphene: a new carbon allotrope, *Proc. Natl. Acad. Sci. U. S. A.*, 2015, **112**, 2372-2377.

2. Y. Shen and Q. Wang, Pentagon-based 2D materials: Classification, properties and applications, *Phys. Rep.*, 2022, **964**, 1-42.

3. M. A. Nazir, A. Hassan, Y. Shen and Q. Wang, Research progress on penta-graphene and its related materials: Properties and applications, *Nano Today*, 2022, **44**, 101501.

4. M. Yagmurcukardes, H. Sahin, J. Kang, E. Torun, F. M. Peeters and R. T. Senger, Pentagonal monolayer crystals of carbon, boron nitride, and silver azide, *J. Appl. Phys.*, 2015, **118**, 104303.

5. J. Li, X. Fan, Y. Wei and G. Chen, Penta-B_xN_y sheet: a density functional theory study of two-dimensional material, *Sci. Rep.*, 2016, **6**, 31840.

6. L.-S. Zhao, Y. Wang, C.-P. Chen, L.-L. Liu, H.-X. Yu, Y. Zhang, Y. Chen and X.-C. Wang, Elastic, electronic and optical properties of stable pentagonal ZnO_2, *Physica E*, 2017, **91**, 82-87.

7. G. Liu, Q. Zeng, P. Zhu, R. Quhe and P. Lu, Negative Poisson's ratio in monolayer $PdSe_2$, *Comput. Mater. Sci.*, 2019, **160**, 309-314.

8. C. Long, Y. Liang, H. Jin, B. Huang and Y. Dai, $PdSe_2$: Flexible two-dimensional transition metal dichalcogenides monolayer for water splitting photocatalyst with extremely low recombination rate, *ACS Appl. Energy Mater.*, 2018, **2**, 513-520.

9. S. Yuan, Q. Zhou, Q. Wu, Y. Zhang, Q. Chen, J.-M. Hou and J. Wang, Prediction of a room-temperature eight-coordinate two-dimensional topological insulator: penta-RuS_4 monolayer, *npj 2D Materials and Applications*, 2017, **1**, 29.

10. X. Li, S. Meng and J.-T. Sun, Emergence of d-orbital magnetic Dirac fermions in a MoS_2 monolayer with squared pentagon structure, *Phys. Rev. B*, 2020, **101**, 144409.

11. R.-W. Zhang, C.-C. Liu, D.-S. Ma and Y. Yao, From node-line semimetals to large-gap quantum spin Hall states in a family of pentagonal group-IVA chalcogenide, *Phys. Rev. B*, 2018, **97**, 125312.

12. K. Zhao and Q. Wang, High Curie temperature ferromagnetism in penta-MnN_2 monolayer, *Appl. Surf. Sci.*, 2020, **505**, 144620.

13. L. Liu, I. Kankam and H. L. Zhuang, Single-layer antiferromagnetic semiconductor CoS_2 with pentagonal structure, *Phys. Rev. B*, 2018, **98**, 205425.

14. W. Zhang, Y. Cui, C. Zhu, B. Huang and S. Yan, Flexible ferroelasticity in monolayer PdS_2: a DFT study, *Phys. Chem. Chem. Phys.*, 2021, **23**, 10551-10559.

15. K. Zhao, Y. Guo, Y. Shen, Q. Wang, Y. Kawazoe and P. Jena, Penta-BCN: A new ternary pentagonal monolayer with intrinsic piezoelectricity, *J. Phys. Chem. Lett.*, 2020, **11**, 3501-3506.

16. T. Thanasarnsurapong, K. Dabsamut, T. Maluangnont, J. T-Thienprasert, S. Jungthawan and A. Boonchun, Piezoelectric and electronic properties of hydrogenated penta-BCN: A computational study, *J. Appl. Phys.*, 2021, **129**, 095101.

17. W. Sun, Y. Shen, Y. Guo, Y. Chen and Q. Wang, 1,2,4-Azadiphosphole-based piezoelectric penta-CNP sheet with high spontaneous polarization, *Appl. Surf. Sci.*, 2021, **554**, 149499.

18. Y. G. Guo, J. Zhou, H. H. Xie, Y. Y. Chen and Q. Wang, Screening transition metal-based polar pentagonal monolayers with large piezoelectricity and shift current, *npj Comput. Mater.*, 2022, **8**, 40.

19. Y. Shen, Y. Guo and Q. Wang, Large out-of-plane second harmonic generation susceptibility in penta-ZnS_2 sheet, *Adv. Theory Simul.*, 2020, **3**, 2000027.

20. J. I. Cerdá, J. Slawinska, G. Le Lay, A. C. Marele, J. M. Gomez-Rodriguez and M. E. Davila, Unveiling the pentagonal nature of perfectly aligned single-and double-strand Si nano-ribbons on Ag(110), *Nat. Commun.*, 2016, **7**, 13076.

21. W. L. Chow, P. Yu, F. Liu, J. Hong, X. Wang, Q. Zeng, C. H. Hsu, C. Zhu, J. Zhou, X. Wang, J. Xia, J. Yan, Y. Chen, D. Wu, T. Yu, Z. Shen, H. Lin, C. Jin, B. K. Tay and Z. Liu, High mobility 2D palladium diselenide field-effect transistors with tunable ambipolar characteristics, *Adv. Mater.*, 2017, **29**, 1602969.

22. A. D. Oyedele, S. Yang, L. Liang, A. A. Puretzky, K. Wang, J. Zhang, P. Yu, P. R. Pudasaini, A. W. Ghosh, Z. Liu, C. M. Rouleau, B. G. Sumpter, M. F. Chisholm, W. Zhou, P. D. Rack, D. B. Geohegan and K. Xiao, $PdSe_2$: pentagonal two-dimensional layers with high air stability for electronics, *J. Am. Chem. Soc.*, 2017, **139**, 14090-14097.

23. Y. Gu, H. Cai, J. Dong, Y. Yu, A. N. Hoffman, C. Liu, A. D. Oyedele, Y. C. Lin, Z. Ge, A. A. Puretzky, G. Duscher, M. F. Chisholm, P. D. Rack, C. M. Rouleau, Z. Gai, X. Meng, F. Ding, D. B. Geohegan and K. Xiao, Two-dimensional palladium diselenide with strong in-plane optical anisotropy and high mobility grown by chemical vapor deposition, *Adv. Mater.*, 2020, **32**, e1906238.

24. E. Li, D. Wang, P. Fan, R. Zhang, Y.-Y. Zhang, G. Li, J. Mao, Y. Wang, X. Lin, S. Du and H.-J. Gao, Construction of bilayer $PdSe_2$ on epitaxial graphene, *Nano Res.*, 2018, **11**, 5858–5865.

25. X. Zhang, G. Su, J. Lu, W. Yang, W. Zhuang, K. Han, X. Wang, Y. Wan, X. Yu and P. Yang, Centimeter-scale few-layer PdS_2: Fabrication and physical properties, *ACS Appl. Mater. Interfaces*, 2021, **13**, 43063-43074.

26. M. Bykov, E. Bykova, A. V. Ponomareva, F. Tasnadi, S. Chariton, V. B. Prakapenka, K. Glazyrin, J. S. Smith, M. F. Mahmood, I. A. Abrikosov and A. F. Goncharov, Realization of an ideal cairo tessellation in nickel diazenide NiN_2: High-pressure route to pentagonal 2D materials, *ACS Nano*, 2021, **15**, 13539-13546.

27. S. Wei, S. Zheng, X. Wen, C. Xie and J. Liang, A novel antiferromagnetic semiconductor hidden in pyrite, *Comput. Mater. Sci.*, 2020, **183**, 109852.

28. A. B. Puthirath, A. P. Balan, E. F. Oliveira, V. Sreepal, F. C. Robles Hernandez, G. Gao, N. Chakingal, L. M. Sassi, P. Thibeorchews, G. Costin, R. Vajtai, D. S. Galvao, R. R. Nair and P. M. Ajayan, Apparent ferromagnetism in exfoliated ultrathin pyrite sheets, *J. Phys. Chem. C*, 2021, **125**, 18927-18935.

29. L. Liu and H. L. Zhuang, PtP_2: An example of exploring the hidden Cairo tessellation in the pyrite structure for discovering novel two-dimensional materials, *Phys. Rev. Mater.*, 2018, **2**, 114003.

30. H. L. Zhuang, From pentagonal geometries to two-dimensional materials, *Comput. Mater. Sci.*, 2019, **159**, 448-453.

31. X. Lv, L. Yu, F. Li, J. Gong, Y. He and Z. Chen, Penta-MS_2 (M = Mn, Ni, Cu/Ag and Zn/Cd) monolayers with negative Poisson's ratios and tunable bandgaps as water-splitting photocatalysts, *J. Mater. Chem. A*, 2021, **9**, 6993-7004.

32. X. Liu, T. Ouyang, D. Zhang, H. Huang, H. Wang, H. Wang and Y. Ni, First-principles calculations of phonon transport in two-dimensional penta-X_2C family, *J. Appl. Phys.*, 2020, **127**, 205106.

33. Y.-S. Lan, X.-R. Chen, C.-E. Hu, Y. Cheng and Q.-F. Chen, Penta-PdX_2 (X = S, Se, Te) monolayers: promising anisotropic thermoelectric materials, *J. Mater. Chem. A*, 2019, **7**, 11134-11142.

34. W. L. Tao, Y. Q. Zhao, Z. Y. Zeng, X. R. Chen and H. Y. Geng, Anisotropic

thermoelectric materials: Pentagonal PtM$_2$ (M = S, Se, Te), *ACS Appl. Mater. Interfaces*, 2021, **13**, 8700-8709.

35. G. Yang, R. Niu, L. Sang, X. Liao, D. R. G. Mitchell, N. Ye, J. Pei, J. F. Li and X. Wang, Ultra-high thermoelectric performance in bulk BiSbTe/amorphous boron composites with nano-defect architectures, *Adv. Energy Mater.*, 2020, **10**, 2000757.

36. X.-L. Shi, W.-Y. Chen, T. Zhang, J. Zou and Z.-G. Chen, Fiber-based thermoelectrics for solid, portable, and wearable electronics, *Energy Environ. Sci.*, 2021, **14**, 729-764.

37. X. L. Shi, W. D. Liu, M. Li, Q. Sun, S. D. Xu, D. Du, J. Zou and Z. G. Chen, A solvothermal synthetic environmental design for high-performance SnSe-based thermoelectric materials, *Adv. Energy Mater.*, 2022, **12**, 2200670.

38. G. Kresse and J. Furthmuller, Efficient iterative schemes for ab initio total-energy calculations using a plane-wave basis set, *Phys. Rev. B*, 1996, **54**, 11169-11186.

39. G. Kresse and J. Furthmuller, Efficiency of ab-initio total energy calculations for metals and semiconductors using a plane-wave basis set, *Comput. Mater. Sci.*, 1996, **6**, 15-50.

40. P. E. Blöchl, Projector augmented-wave method, *Phys. Rev. B*, 1994, **50**, 17953-17979.

41. M. P. Teter, M. C. Payne and D. C. Allan, Solution of Schrodinger-equation for large systems, *Phys. Rev. B*, 1989, **40**, 12255-12263.

42. J. P. Perdew, K. Burke and M. Ernzerhof, Generalized gradient approximation made simple, *Phys. Rev. Lett.*, 1996, **77**, 3865-3868.

43. J. Heyd, G. E. Scuseria and M. Ernzerhof, Hybrid functionals based on a screened Coulomb potential, *J. Chem. Phys.*, 2003, **118**, 8207-8215.

44. J. Heyd, G. E. Scuseria and M. Ernzerhof, Erratum: "Hybrid functionals based on a screened Coulomb potential.", *J. Chem. Phys.*, 2006, **124**, 219906.

45. S. Nosé, A unified formulation of the constant temperature molecular dynamics methods, *J. Chem. Phys.*, 1984, **81**, 511-519.

46. G. K. H. Madsen, J. Carrete and M. J. Verstraete, BoltzTraP2, a program for interpolating band structures and calculating semi-classical transport coefficients, *Comput. Phys. Commun.*, 2018, **231**, 140-145.

47. M. Omini and A. Sparavigna, An iterative approach to the phonon Boltzmann-equation in the theory of thermal-conductivity, *Phys. B*, 1995, **212**, 101-112.

48. W. Li, J. Carrete, N. A. Katcho and N. Mingo, ShengBTE: A solver of the Boltzmann transport equation for phonons, *Comput. Phys. Commun.*, 2014, **185**, 1747-1758.

49. A. Togo and I. Tanaka, First principles phonon calculations in materials science, *Scripta Mater.*, 2015, **108**, 1-5.

50. F. Eriksson, E. Fransson and P. Erhart, The Hiphive package for the extraction of high-order force constants by machine learning, *Adv. Theory Simul.*, 2019, **2**, 1800184.

51. A. Jain, S. P. Ong, G. Hautier, W. Chen, W. D. Richards, S. Dacek, S. Cholia, D.

Gunter, D. Skinner, G. Ceder and K. A. Persson, Commentary: The Materials Project: A materials genome approach to accelerating materials innovation, *APL Mater.*, 2013, **1**, 011002.

52. S. S. Chou, N. Sai, P. Lu, E. N. Coker, S. Liu, K. Artyushkova, T. S. Luk, B. Kaehr and C. J. Brinker, Understanding catalysis in a multiphasic two-dimensional transition metal dichalcogenide, *Nat. Commun.*, 2015, **6**, 8311.

53. S. Zhang, J. Zhou, Q. Wang and P. Jena, Beyond graphitic carbon nitride: nitrogen-rich penta-CN_2 sheet, *J. Phys. Chem. C*, 2016, **120**, 3993-3998.

54. Y. Guo, C. Zhang, J. Zhou, Q. Wang and P. Jena, Lattice dynamic and instability in pentasilicene: A light single-element ferroelectric material with high Curie temperature, *Phys. Rev. Appl.*, 2019, **11**, 064063.

55. L. Liu and H. L. Zhuang, Computational prediction and characterization of two-dimensional pentagonal arsenopyrite FeAsS, *Comput. Mater. Sci.*, 2019, **166**, 105-110.

56. W. Voigt, *Lehrbuch der kristallphysik (mit ausschluss der kristalloptik)*, Springer-Verlag, 2014.

57. M. Born and K. Huang, *Dynamical theory of crystal lattices*, Clarendon press, 1954.

58. Z.-L. Lv, H.-L. Cui, H. Wang and G.-F. Ji, First principles study on the electronic, elastic and vibrational properties of marcasite-type OsP_2, *Comput. Mater. Sci.*, 2016, **121**, 54-60.

59. Y. C. Wang, L. F. Yu, F. Zhang, Q. Chen, Y. Q. Zhan, L. W. Meng, X. Zheng, H. M. Wang, Z. Z. Qin and G. Z. Qin, The consistent behavior of negative Poisson's ratio with interlayer interactions, *Mater. Adv.*, 2022, **3**, 4334-4341.

60. G. Henkelman, A. Arnaldsson and H. Jónsson, A fast and robust algorithm for Bader decomposition of charge density, *Compu. Mater. Sci.*, 2006, **36**, 354-360.

61. H. Lang, S. Zhang and Z. Liu, Mobility anisotropy of two-dimensional semiconductors, *Phys. Rev. B*, 2016, **94**, 235306.

62. Y. Wang, Y. Li and Z. Chen, Not your familiar two dimensional transition metal disulfide: structural and electronic properties of the PdS_2 monolayer, *J. Mater. Chem. C*, 2015, **3**, 9603-9608.

63. L. F. Huang, P. L. Gong and Z. Zeng, Correlation between structure, phonon spectra, thermal expansion, and thermomechanics of single-layer MoS_2, *Phys. Rev. B*, 2014, **90**, 045409.

64. W. J. Qiu, L. L. Xi, P. Wei, X. Z. Ke, J. H. Yang and W. Q. Zhang, Part-crystalline part-liquid state and rattling-like thermal damping in materials with chemical-bond hierarchy, *Proc. Natl. Acad. Sci. U. S. A.*, 2014, **111**, 15031-15035.

65. H. S. Kim, Z. M. Gibbs, Y. L. Tang, H. Wang and G. J. Snyder, Characterization of Lorenz number with Seebeck coefficient measurement, *APL Mater.*, 2015, **3**, 041506.

66. T. Ouyang, E. L. Jiang, C. Tang, J. Li, C. Y. He and J. X. Zhong, Thermal and thermoelectric properties of monolayer indium triphosphide (InP_3): a first-principles study, *J. Mater. Chem. A*, 2018, **6**, 21532-21541.

67. Y. Chen, Y. Shen, X. Li, J. Sun and Q. Wang, *β*-CsCu$_5$Se$_3$: A promising thermoelectric material going beyond photovoltaic application, *Adv. Theory Simul.*, 2020, **3**, 2000169.

Journal of Materials Chemistry A Accepted Manuscript